UAV Icing: Experimental Investigation and Numerical CHT Simulations of a Propeller Ice Protection System

Markus Frey[1] and Nicolas Carlo Müller[2]
Norwegian University of Science and Technology, Trondheim, Trøndelag, 7491, Norway

Joachim Wallisch[3]
Norwegian University of Science and Technology, Trondheim, Trøndelag, 7491, Norway

Richard Hann[4]
Norwegian University of Science and Technology, Trondheim, Trøndelag, 7491, Norway

In-flight icing on unmanned aerial vehicle (UAV) propellers can lead to severe aerodynamic performance degradation or even complete loss of the UAV. Ice protection systems (IPS) are used to enable the flight of UAVs in icing conditions by protection aerodynamically critical surfaces such as wings and propellers. In this study an electro-thermal ice protection system is studied for the propeller of a small-medium fixed-wing UAV. This study aims to optimize the electro-thermal IPS design to increase efficiency and reduce the required power of the propeller IPS using numerical conjugated heat transfer (CHT) simulations within ANSYS FENSAP-ICE. The numerical simulations are validated using existing literature values and new experimental data acquired in icing wind tunnel tests. The conditions of the simulations and experiments are representative for realistic and critical in-flight conditions to examine the ETIPS performance, the required heat fluxes and temperature distributions for a better understanding of the underlying phenomena during the process of anti-icing. This is important to improve already existing ETIPS setups by enlarging the heated area and improve the internal temperature distribution by integrating a highly thermally conductive layer. These approaches lay the foundation for future ETIPS and enable UAVs to operate in potential icing conditions.

[1] Student, Department of Engineering Cybernetics, NTNU, and AIAA Student Member, markfr@stud.ntnu.no
[1] Student, University of Stuttgart, and AIAA Student Member, st154842@stud.uni-stuttgart.de
[2] PhD candidate, UAV Icing Lab, Department of Engineering Cybernetics, NTNU, and AIAA Student Member, nicolas.c.muller@ntnu.no
[2] Aerodynamics Engineer, UBIQ Aerospace, and AIAA Student Member
[3] PhD candidate, UAV Icing Lab, Department of Engineering Cybernetics, NTNU, and AIAA Student Member, joachim.wallisch@ntnu.no
[3] Aerodynamics Engineer, UBIQ Aerospace, and AIAA Student Member
[4] Senior Researcher, UAV Icing Lab, Department of Engineering Cybernetics, NTNU, and AIAA Member. richard.hann@ntnu.no
[4] Lead Aerodynamics Engineer, UBIQ Aerospace, and AIAA Member

I. Nomenclature

AOA	=	angle of attack
CFD	=	computational fluid dynamics
CHT	=	conjugate heat transfer
HF	=	heat flux
HTC	=	heat transfer coefficient
IPS	=	ice protection system
ETIPS	=	electro-thermal ice protection system
LWC	=	liquid water content
MVD	=	mean volume diameter
NRMS	=	normalized root mean square
UAV	=	unmanned/uncrewed aerial vehicle, drone
k	=	heat conductivity
k_{equ}	=	equivalent heat conductivity
k_x, k_y	=	original heat conductivity in x and y direction
r	=	refinement ratio
x, y	=	cartesian coordinates
$\tilde{x}$, $\tilde{y}$	=	equivalent cartesian coordinates
y^+	=	dimensionless wall distance

II. Introduction

Atmospheric in-flight icing on the surfaces of unmanned or uncrewed aerial vehicles (UAVs), also known as drones or unmanned aircraft systems (UAS), particularly on propellers, will lead to severe flight performance degradation or even complete loss of control [1] [2]. In addition to manned aviation, unmanned aviation represents an emerging technology that is gaining in importance [3]. UAVs are used in commercial, military, research and search and rescue (SAR) applications [4]. The focus in this work is on small-medium fixed-wing UAVs with a maximum take-off weight of around 25 kg. Especially, in recent years, UAVs have been increasingly used in the field of delivering medications and first aid packages to highly remote and inaccessible locations [5]. A variety of these locations are situated in extreme northern latitudes, where the land routes are often cut off by heavy snow and ice, with no suitably lading site for large aircraft [5]. The accessibility by UAVs is often the faster and cheaper way to assist in emergencies to the people living there [6]. To reliably perform these tasks, UAVs must operate in the most challenging weather conditions. These weather conditions not only occur on a few locations, inflight icing can happen all year around the globe [7]. One of the greatest dangers occurs when flying through a cloud containing supercooled droplets [8]. These droplets freeze immediately when impinging on any surface. The resulting ice formation can lead to significant limitations in flight capability and controllability [1]. The ice accretion on static parts such as the airframe and wings must be distinguished from the dynamic parts such as all of propulsion devices like propellers. On wings the accumulated ice enlarges the surface, changes the aerodynamic shape, and increases the weight of the UAV [9]. This usually leads to a decreased lift and increased drag [10]. Propellers are even more sensitive to ice accretion due to their smaller size and high rotation rate [1]. The consequence is a substantial reduction in thrust generation and increased torque over very short icing durations [11]. In response to these dangers, ice protection systems (IPS) have been developed. While IPS for manned aviation have been well established for some time, adapting these systems for UAVs has presented unique challenges due to limited energy availability and strict mass constraints in small-medium UAVs [12].

While icing research in manned aviation has a long history dating back to the 1940s, the study of icing on UAVs began much later due to technological complexities and initial focus on autonomous flight capabilities [10]. Icing on rotating parts have been well investigated on rotors of helicopters and rotors of wind turbines [13]. Research on UAVs has only recently become more active and most papers focus on airfoils only [14]. Just a few examinations have been done on icing of UAV propellers, rotors [15] or the electric propulsion system [16]. Experimental studies of ice accretion on propellers show several hazards. Besides the rapid loss of thrust, significant more power is required to maintain rotational speed due to increased torque [17]. The different relative speeds along the propeller blade lead to ice accumulations in shapes of chunks and the location is less predictable than for static parts like wings [11]. These chunks represent a special problem which clarifies the necessity of IPS even more. The random appearance of the ice chunks lead to imbalances in the propeller weight distribution that causes massive forces and vibrations acting on the whole system. In addition, the centrifugal forces created by the propeller lead to ice shedding [18]. Ice shedding describes the event when adhesion forces between the ice and the propeller surface are not strong enough and the

accumulated ice breaks off. The shedding ice not only causes further vibrational forces but also poses danger for the whole UAV.

The solution for this hazard due to ice accretion is the use of ice protection systems. The IPS for UAVs can generally be categorized into passive and active systems [19]. Passive systems utilize surface coatings to prevent ice accretion, whereas active systems primarily employ heat to prevent ice buildup or cyclically remove ice from the UAV's surfaces. Passive coatings have shown promise, particularly in rotor applications, by reducing ice adhesion forces and facilitating ice shedding [20]. In contrast, active systems, often referred to as electro-thermal ice protection systems (ETIPS), have been developed for various UAV components, including wings, propellers and rotors. ETIPS work with the principle of resistive heating and requires an additional power supply. Those systems can be operated in anti-icing modes and de-icing mode [21]. In anti-icing mode, the systems heat the structure continuously to prevent any water on the surface from freezing. In contrast, the de-icing mode allows an uncritical amount of ice to form which is then periodically removed. Recent investigations by Müller et al. [17] offers promising results in the development of an ETIPS anti-icing for propeller of a small-medium fixed wing UAV. The result was an ETIPS integrated into the propellers leading edge separated into two parts in spanwise direction.

One critical aspect often overlooked in the investigation of anti-icing, is the thermal impact on the propeller structure and materials. Particularly in smaller UAVs that rely on composite propellers for thrust. Composite materials show many advantages in comparison to metallic alternatives [22]. On the one hand, composites are lightweight while keeping high stiffness and strength on the other hand. Due to the availability of various combinations of fibers and resins resulting in distinct material properties, along with the flexibility of utilizing different layup configurations, the properties can be further optimized. In addition, composites are insensitive to corrosion and show a high grade of design flexibility due to the manufacturing process. However, they are sensitive to high structural temperatures. An limitation of a thermal IPS regarding composite structures is the maximal glass transition temperatures of the resin [23]. The glass transition temperature in general describes the temperature at which a material changes from a glass solid state to a rubbery state. This transition influences mainly the materials' mechanical, thermal and electrical properties [24]. For propeller applications, the most critical aspects are the change in stiffness and strength that may cause deformations and material instabilities followed by performance degradation or even complete loss of the propeller. The delicate balance between keeping the propeller ice-free through electro-thermal heating and maintaining the structural integrity of composite materials, presents a significant challenge.

This work focuses on experimental and numerical investigations of the internal structural temperature distribution, aiming to enhance the design of an existing anti-icing IPS. The goal is not only to keep the propeller surface free of ice but also to maintain low internal temperatures to preserve the structural integrity of composite materials. By addressing these challenges, this research contributes to the advancement of ice protection systems for UAVs, ultimately improving their operational safety in icing conditions.

This study builds upon prior research conducted by Müller et al. [17] and introduces thermistors integrated into protected propellers, enabling a more comprehensive analysis of temperature behavior within the propeller structure. The propeller material, a composite with a low-temperature threshold, necessitates optimization of the ETIPS design to prevent damage from excessive temperatures while maintaining sufficient heat flux for effective anti-icing. Striking a balance between propeller protection and anti-icing effectiveness is a critical aspect of this study. Numerical simulations are performed to predict temperature distributions within the propeller, which is instrumental in the development of optimized ETIPS [25]. These simulations are conducted using icing computational fluid dynamics (CFD) methods and conjugate heat transfer (CHT) methods in ANSYS FENSAP-ICE [26]. The simulations are validated on literature and experimental data from icing wind tunnel tests. The study aims to provide insights into the performance of ETIPS under realistic and challenging in-flight conditions, helping to refine existing setups and enable UAVs to operate safely in potential icing conditions.

III. Methods

A. Numerical methods and analysis

To perform the numerical simulations, the software ANSYS FENSAP-ICE (version 2022R2) with the built-in modules FENSAP, DROP3D, ICE3D, C3D and CHT3D is used [26]. This advanced CFD code can be used for calculating in-flight icing on UAVs. The flow solver FENSAP uses the approach of Reynolds Averaged Navier-Stokes equations [27]. The droplet trajectories and impingements on the surface are calculated by the module DROP3D using an Eulerian approach [28]. The next step is to calculate the ice accretion over a specific time range. The FENSAP-ICE module ICE3D uses the Messinger model and describes the effect of ice accretion with a series of partial differential equations of conservation [29]. For the prediction of the internal heat conductivity and temperature distribution, the module C3D is used. The module is able to differentiate between several materials in steady and

unsteady cases by a partial differential equation [26]. All these modules are merged into the CHT3D module to calculate temperature exchanges between solids and fluids iteratively [30].

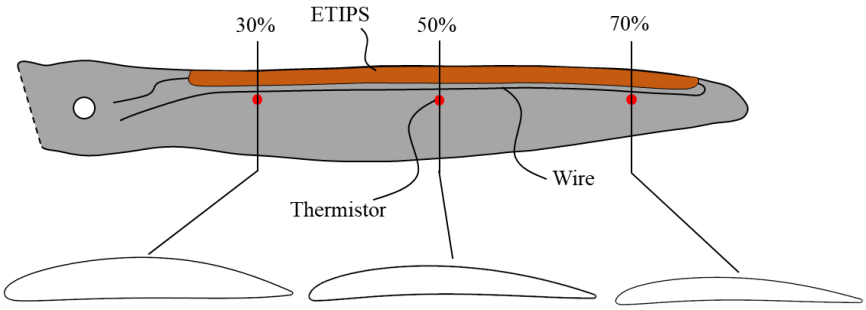

Fig. 1 Sketch of the 21x13 propeller with ETIPS and the three propeller sections.

In this study, simulations were done for two different geometries. The first CHT-simulations for validating these simulations were done on a NACA 0012 airfoil, since only few studies on propellers are available. The airfoil data was obtained from a database called airfoil tools [31] with a chord length of 1 m. The airfoil was cut at a chord length of 0.9144 m to generate a blunt trailing edge to avoid numerical issues. The final results and examinations of temperature distributions were done on the geometry of a 21-inch propeller from Mejzlik [32]. For the 2D propeller simulations, three cross-sections of the propeller were created using Siemens NX [33] as shown in Fig. 1. The sections were taken at 30%, 50% and 70% of the blade radius, to agree with the thermistor positions during the experimental tests to examine the differences along the propeller radius. The chord length of each section was examined geometrically between the two points with the biggest distance. The relevant propeller data and differences between the three sections are shown in Table 1.

Table 1 Propeller data at each propeller section.

Propeller section	Radial distance [m]	Chord length [m]	Pitch angle [°]
30%	0.0800	0.0407	31.31
50%	0.1334	0.0405	23.38
70%	0.1867	0.0330	17.78

All simulations are performed in 2D and the grids are generated by using the software Pointwise 2022.2.2 [34]. For CHT-simulations, two grids are required. The two propeller grids for the 70% section can be seen in Fig. 2 and Fig. 3. The flow-grid is necessary for simulating the flow field around and at the surface of the airfoil. The second solid-grid provides the internal structure of the airfoil for simulating heat conduction. The flow-grid is generated as an O-type having a far-field size of 100 times the airfoil chord length to avoid boundary influences. The grid inside this circle is mainly unstructured except near the surface. Near the surface, the T-Rex function from Pointwise is applied to enhance grid quality and density in critical areas, such as near walls or geometries with high curvature. The T-Rex mesh consists of 600 layers of triangles and quads starting at the surface with an initial cell height of 10^{-6} m and a growth rate of 1.2 to achieve a dimensionless wall distance of $y^+<1$. This requirement ensures that the mesh is fine enough to accurately simulate the boundary layer, which is crucial for analyzing momentum and heat transfer at the surface.

The solid-grid is formed by extracting the grid points directly located at the surface from the previously established flow-grid. For generating the internal mesh two methods are used. The basic method uses the pointwise function ‘normal extrusion’ enabling generating layer-by-layer normal to the surface. This method is suitable for the first two to three layers right if they are generally thin (e.g. right below the airfoil surface). For thicker layers at positions of high curvature like at the leading edge the layers start to thicken up, generating unrealistic layers. To prevent this, the internal boundaries of the layers and structures, especially for propeller simulations, were generated in the CAD software Siemens NX [33] in advance. Afterwards, the generated layers were equipped with grid points to generate meshes in Pointwise.

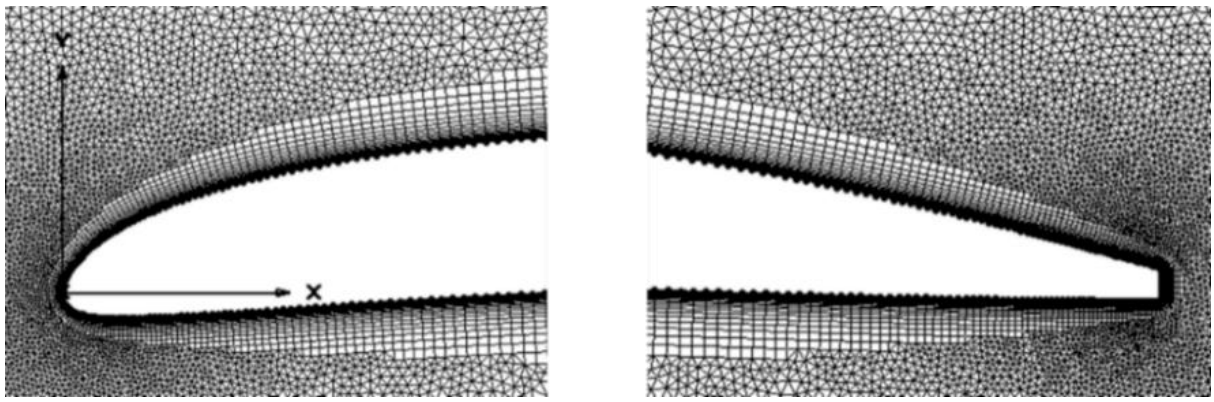

Fig. 2 Flow-grid at 70% radius cross section of the propeller.

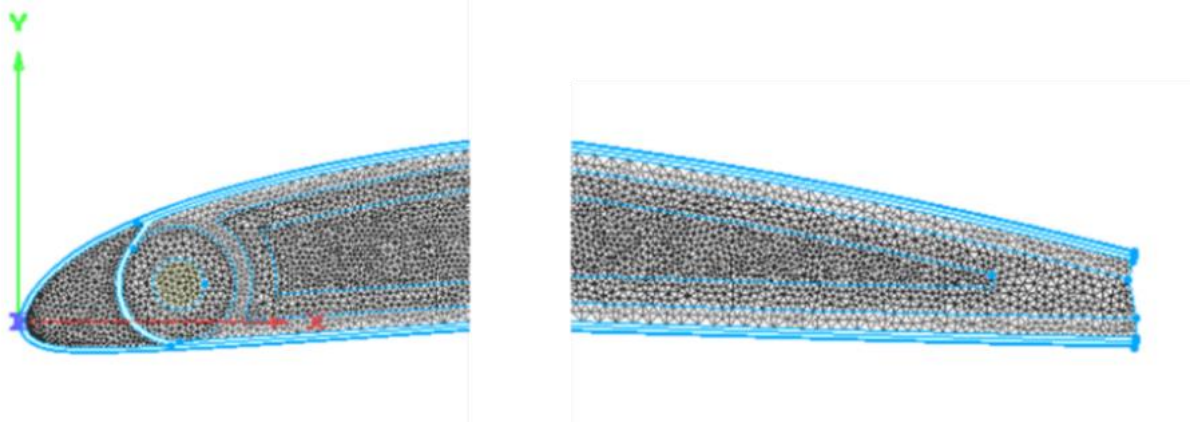

Fig. 3 Solid-grid at 70% radius cross section of the propeller.

For both geometries, a grid-dependence study was performed to obtain the optimal mesh resolution. Four flow-grids with a refinement ratio of $r = \sqrt{2}$ and three solid-grids are compared in order to find the best possible grid for the applications. For the flow-grids, comparisons were done regarding the aerodynamic parameters of lift- and drag-coefficient and the heat transfer coefficient at the surface of the airfoils. Considering the solid-grids, the surface mesh resolutions of the three least fine flow-grids are used to generate the solid-grids. Evaluation of the solid-grids are done by comparison of the surface temperatures. To evaluate the differences of the outcomes, several methods are possible. For the aerodynamic values of lift- and drag-coefficient a Richardson extrapolation [35] was used to observe the convergence, while for the other values the normalized root mean square [36] (NRMS) approach was applied. The NRMS function describes the deviation between the values of a grid and the mean values of the finest grid. The flow-grid features for the NACA 0012 airfoil can be seen in Table 2 and for the propeller grids in Table 3.

Table 2 Flow-grid features of the NACA 0012 airfoil.

	Coarse	Medium	Fine	xFine
Points on lower and upper side	180	255	360	510
Leading edge spacing [mm]	0.60	0.40	0.30	0.20
Trailing edge spacing [mm]	0.50	0.30	0.25	0.15
Points on far field	200	283	400	566

Table 3 Flow-grid features of the propeller grids.

	Coarse	Medium	Fine	xFine
Points on lower and upper side	280	400	560	790
Leading edge spacing [mm]	$7{\cdot}10^{-5}$	$5{\cdot}10^{-5}$	$3.5{\cdot}10^{-5}$	$2.4{\cdot}10^{-5}$
Trailing edge spacing [mm]	$7{\cdot}10^{-5}$	$5{\cdot}10^{-5}$	$3.5{\cdot}10^{-5}$	$2.4{\cdot}10^{-5}$
Points on far field	280	400	560	790

B. Analytical approaches

Composite materials show differences in heat conduction dependent on how the fibers are layered. Usually, the heat conductivity reaches higher values in fiber direction than normal to it. FENSAP-ICE is not able to take into account anisotropic heat conductivity. Therefore, an analytical approach by Ohmura et al. [37] was applied to calculate an equivalent (equ) thermal conductivity k_{equ} and equivalent material lengths $\tilde{x}$ and $\tilde{y}$ based on the hot-wire method. The equivalent values can be calculated as follows:

$$\tilde{x} = \sqrt{\frac{k_{\mathrm{equ}}}{k_{\mathrm{x}}}}x \text{ and } \tilde{y} = \sqrt{\frac{k_{\mathrm{equ}}}{k_{\mathrm{y}}}}y \tag{1}$$

$$k_{\mathrm{equ}} = \sqrt{k_{\mathrm{x}}k_{\mathrm{y}}} \tag{2}$$

With k_{x} and k_y as the heat conductivity values in the original x and y direction.

For the simulations within this work, the composite layup was done in accordance with the propellers that were available for testing. The propeller was made of different composite materials as shown in Fig. 4 with the material values in Table 4. The material properties were provided for this study and got previously examined on the basis of literature and online calculators [38], [39], [40] and [41].

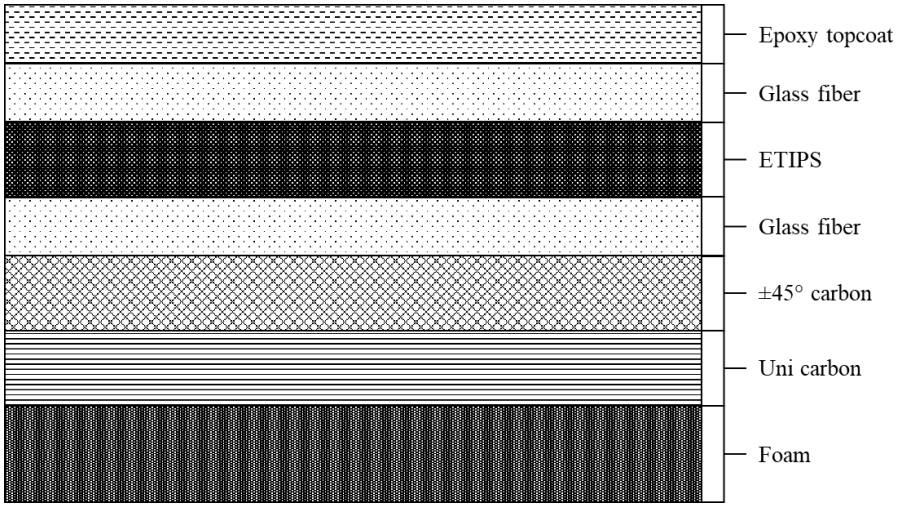

Fig. 4 Propeller composite layup plan at the leading edge without the wire.

Table 4 Composite material values of the propeller.

	Foam	Uni carbon	±45° carbon	Glass fiber	Uni carbon (Heater)	Epoxy topcoat	Copper	Silicone
Layer thickness [mm]	2	0.38	0.18	0.06	0.7	0.02	0.65	0.85
Equivalent thickness [mm]	-	-	0.26	-	-	-	-	-
Density [kg/m^3]	80	1340	1340	1570	1340	1150	8960	1190
Specific heat [J/(kgK)]	1.25	1065	1065	1000	1065	1110	383	1255
Thermal conductivity normal to fiber [W/(mK)]	0.028	0.35	0.65	0.5	0.8	0.18	370	0.25
Thermal conductivity	-	0.35	2.8	0.5	0.6	0.18	-	-

parallel to fiber [W/(mK)]								
Equivalent thermal conductivity [W/(mK)]	-	-	1.35	-	-	-	-	-

The wire to power the ETIPS was placed in the leading edge between the glass fiber and ±45° carbon layers as shown in Fig. 5. Within the propeller setup at three separate locations along the spanwise direction, (30%, 50% and 70%) thermistors were integrated to gain experimental temperature data. The ETIPS in the leading edge of the propeller was extended over 70% - 75% of the propeller diameter.

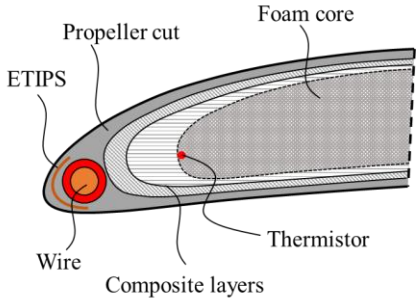

Fig. 5 Schematic sketch of propeller cut leading edge.

The airflow around a propeller is characterized by three different components. The free stream air velocity, the rotation of the propeller and the induced velocity. The simulations in this study are done in 2D and therefore rotation cannot be directly simulated. For each 2D section, the inflow velocity and angle must be calculated previously. The blade element theory was used [42] which calculates the aerodynamic forces on the blade assuming that each blade section acts as a 2D airfoil with the sum of all sections describing the whole propeller. The data for the calculations can be found in Table 5 and the final propeller inflow velocities and angle of attacks for each section in Table 6.

Table 5 Constant values for calculating the propeller flow conditions.

	Air velocity [m/s]	Density [kg/m^3]	Rotation rate [RPM]	Thrust [N]	Area [m^2]
Propeller	25	1.204	4200	12	0.2235

Table 6 Propeller data at each propeller section.

Propeller sections	Inflow velocity [m/s]	Angle of attack [°]
30%	43.83	−5.28
50%	64.21	−0.64
70%	86.17	0.13

C. Experimental setup

An experimental test campaign was performed in order to obtain data for validating the numerical results. The tests were done at the VTT Technical Research Centre in Helsinki, Finland [43]. The icing wind tunnel has an open loop design with a square test section of 70 cm in edge length. Wind speeds of up to 50 m/s with icing conditions of −25 °C can be reached.

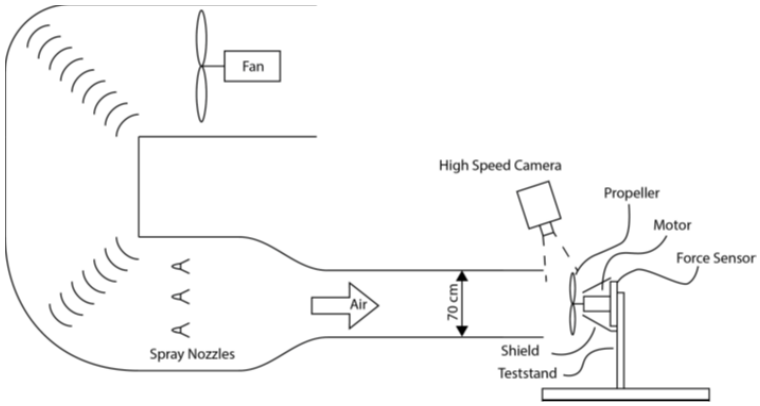

Fig. 6 Test setup at the VTT – icing wind tunnel [18].

As shown in Fig. 6 and Fig. 7, the propeller test stand consists of multiple sensors. The dynamometer "Flight Stand 15" from Tyto Robotics [44] was equipped with an internal torque- and thrust- meter that sends commands directly to the electronic speed controller [45]. An infrared sensor and reflector were used to measure the rotation of the propeller driven by a Hacker Q80-9M motor [46]. A custom-made shield protects all sensible components of the flight test stand from ice accretion and from being hit by shedding ice. The rotation rate was kept constant at 4200 RPM which equals 40 Hz, using a python code. To power the ETIPS, a slip ring [47] was used which was controlled via a control board and pulse width modulation.

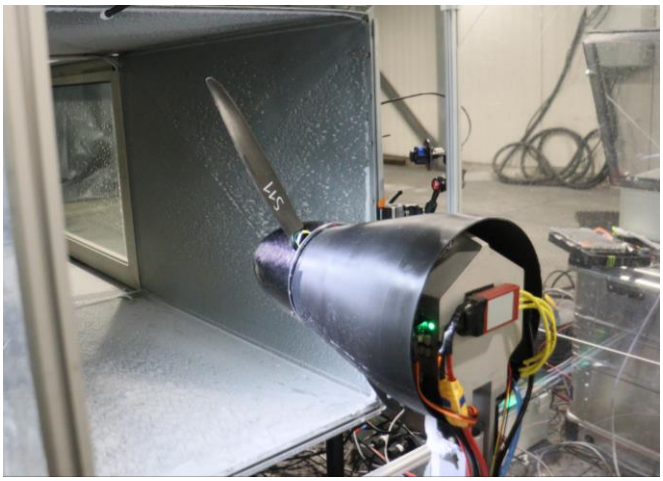

Fig. 7 Picture of propeller test stand.

At the beginning of the test campaign, the liquid water content is calibrated with the method of a rotating cylinder. For the test campaign, two propellers were manufactured with built-in thermistors at three positions along the blade. Experiments were done at two temperatures and different icing conditions but with the same air velocity of 25 m/s and constant propeller rotation rate of 4200 RPM.

Table 7 Test cases of the experimental test campaign.

Test Case	Temperature [°C]	Air velocity [m/s]	LWC [g/m^3]	MVD [µm]	ETIPS power [W]	Run time [s]
#1	−5	25	0.44	20	70	120
#2	−5	25	0	-	50→130 (40 W per 60 s)	180
#3	−10	25	0.44	20	230	120

While test cases #1 and #3 are on wet-conditions, with constant ETIPS power but different temperatures, test case #2 is on dry-conditions with increasing power of 40 W every minute. During the experimental tests, the maximum

ETIPS power was found iteratively. Every run the power was increased gradually to not overheat the internal propeller structure. The limit for internal temperatures measured by the thermistors was set to 60 °C.

IV. Results

A. Validation of CHT-simulations with literature

To first validate the CHT3D simulations, a test campaign from Al-Khalil et al. in 1997 was chosen as reference [48–50]. The objective of their work was to validate NASA´s LEWICE2D and ANTICE computer codes for thermal ice protection systems. This validation was done based on an experimental test campaign on an NACA 0012 airfoil section. The first part [48] of this campaign focuses on the experimental investigation and procedures, the second part [49] on the de-icing test cases and the third part [50] on the anti-icing cases. Chosen as reference was the running wet test case #22 with the numerical setup in accordance to [48].

Before performing the simulations, a grid dependency study was done. Comparing the NRMS values for the flow-grids regarding the heat transfer coefficient, the smallest deviation occurs between the Fine and xFine grids with 0.25% followed by the Medium grid with 0.91% and the Coarse grid with 2.56%. For the solid grids considering the surface temperature, the results are similar with deviations of 0.19% and 0.29% for the Medium and Coarse grids. It turned out that the best compromise between grid resolution and computational effort is reached by the Medium grid.

During the experimental study by Al-Khalil et al. [48,50] it was observed, that the predicted transition from laminar to turbulent flow for the wet cases do not correspond to the experimental observations. This was due to beads and rivulets on the leading edge that forced the transition of the flow, which consequently shows differences in the heat transfer coefficient. It was found that the assumption of a fully turbulent flow with the Spalart Allmaras model showed the best results compared to the literature and was therefore used for the validation [51]. The final validation results in Fig. 8 show good agreement between the FENSAP-ICE simulations and experimental results. This might confirm the choice of the turbulent model and the predicted transition. The biggest differences can be observed at the leading edge, which corresponds to a lower maximal HTC compared to the experiments. Regarding the temperature development over time, the biggest differences can be seen within the first 20 s. The initially set temperature or rather rough time stepping might cause this. Nevertheless, the inner temperature matches the values between 75 s and 200 s closely which indicates that the heat conduction over time must be similar and the material properties and heater powers are chosen correctly. The simulation does not capture the subsequent drop of the experimental examined temperature in the last 100 s for the middle and inner temperature. At the same time, the outer temperature experiences a slight rise. This is expected to be caused by changes during the test, like changes in the power supply or a measurement error, since anti-icing is a stationary case, where such changes cannot happen naturally.

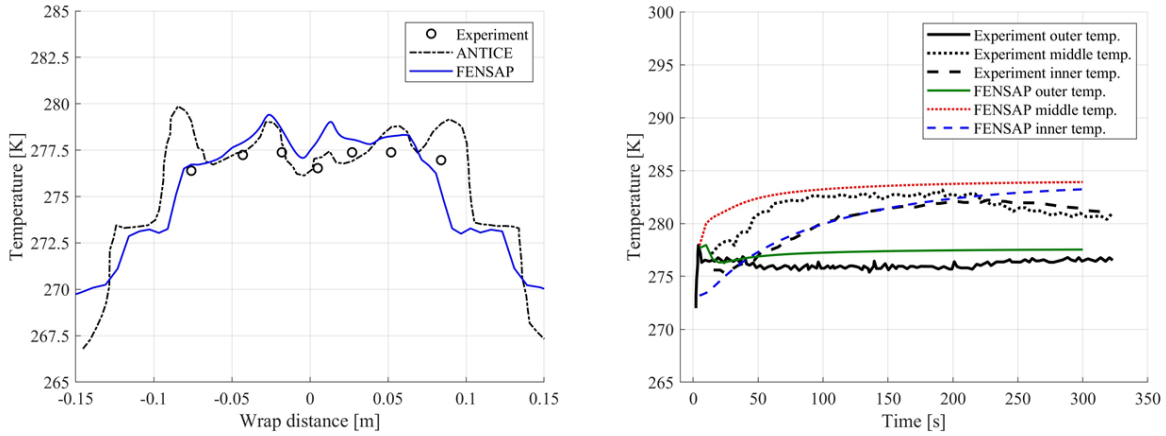

a) **b)**

Fig. 8 Validation results on the surface temperature a) and internal temperature over time b).

B. Validation of 2D CHT-propeller simulations with experiments

As previously done for the NACA 0012 airfoil, a grid dependence study is required for the propeller validation to ensure reliable results independent of the grid. Although three different propeller sections are considered within this work, it was decided to focus on the 70% section for the grid dependency study. Due to the rotation of the propeller, the 70% section being exposed to the highest relative velocity among all three sections, making aerodynamic and

thermodynamic phenomena more sensible to grid resolution. The flow simulations were set up according to Table 5 and Table 6 at −5 °C with an LWC of 0.44 g/m^3. The material values for the CHT-simulation can be found in Table 4 and the ETIPS was powered at $7 \cdot 10^7$ W/m^3. Comparing the heat transfer coefficient values along the propeller surface, all grids show a similar contour (Fig. 9). The observations of just small differences along the surface are confirmed by analyzing the mean differences (NRMS) always referred to the xFine grid with 2.68% for the Fine grid, 3.47% for the Medium grid and 8.55% difference for the Coarse grid. In the comparison of the surface temperature, all grids match each other well. By calculating the mean differences referred to the Fine grid it can be seen that the Coarse grid has a difference of just 0.200% whereas the Medium grid has a difference of just 0.046%. In summary all grids show a sufficient resolution for observing critical spots and flow conditions. Nevertheless, due to the albeit small deviations and the available computational resources it was decided to use the Medium grid for all propeller simulations.

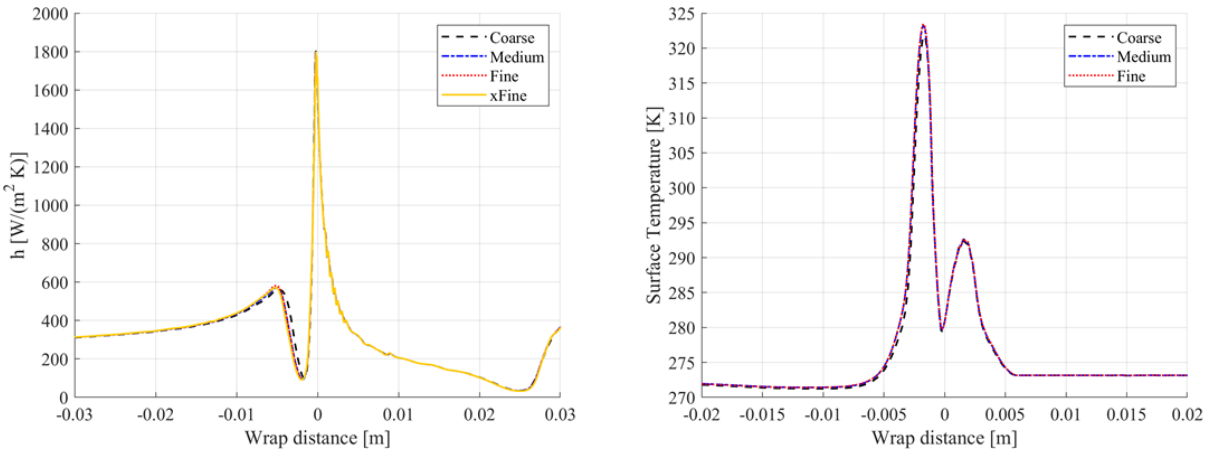

a) **b)**

Fig. 9 Grid resolution comparison of heat transfer coefficient a) and surface temperature b).

The validation of the numerical simulations with the experimental data is a crucial step to verify the accuracy of the numerical results. It provides information about the correctness of the numerical setup, the material properties of the propeller layers and if assumptions like the calculations of the propeller inflows are in an acceptable range. For the experimental research, the propellers were equipped with thermistors positioned at the foremost point of the foam core. Due to manufacturing variations, it was assumed that the thermistor positions vary around 1mm in every direction. Regarding the analyzed propeller sections, all thermistor temperatures obtained from the numerical results are taken at the exact same position. Starting exactly at the front tip of the foam core, for the 50% and 70% section the temperature was taken from the point shifted 0.1 mm in the foam core and not changing the height. For the 30% section the temperature was taken at the position shifted 0.8 mm in the foam core and 0.1 mm downwards.

The propeller validation simulations are performed according to the experimental setup in Table 7. The first validation in Fig. 10 is done with the test cases #1 and #3. The experimental data show two data sets for every propeller section, because thermistors were built in on both blades of the propeller. For the 70% section just one set of data is shown because a wire of one thermistor was cracked right before the first test execution.

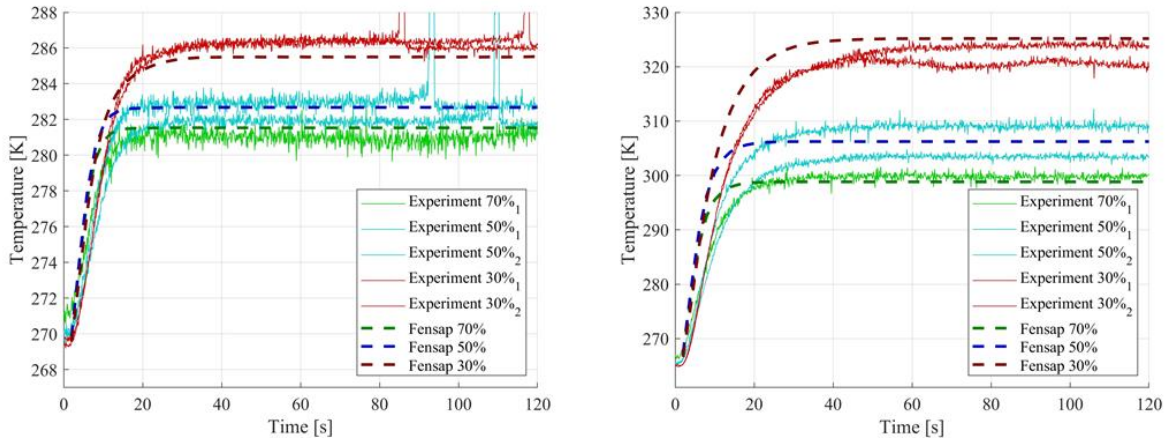

a) **b)**

Fig. 10 Comparison of internal temperature to experimental test case #1 a) and test case #3 b).

It can be seen that the numerical data agree well with the experimental data when steady-state temperatures are reached. Comparing only the experimental data, for the 30% section a bigger difference between the blades can be observed for test case #3 than for test case #1. For the 50% section in both cases, a similar gap occurs between the blades. Causes are described later. Nevertheless, the experimental data show comprehensible results. The biggest observable difference between the numerical and experimental results can be seen in the temperature gradient within the first 15 s – 20 s of the tests. The steady temperature is reached in the numerical results faster than in the experiments. This is more evident in test case #3, where much higher temperatures are generally achieved due to the greater ratio between ambient temperature and heating power. Despite the inaccuracy in the temperature gradient, the reached temperatures of the numerical simulations are in good agreement with the temperatures obtained experimentally. The appearance of runback ice during the experimental investigations for test case #1 can be seen in Fig. 11.

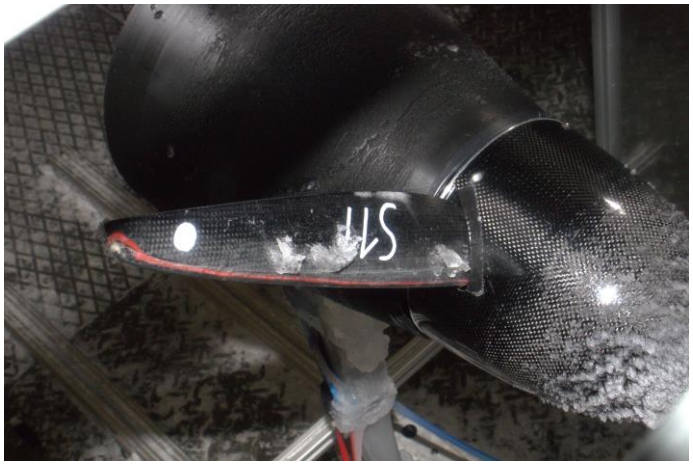

Fig. 11 Runback ice accretion during experiment of test case #1.

To continue with the dry test case #2 as shown in Fig. 12 for the 30% propeller section. To maintain comparability between the dry (#2) and wet (#1, #3) test cases, the stationary anti-icing module of FENSAP-ICE was also used for test case #2. This module is not capable of performing unsteady simulations. For that reason, the dry simulations were performed with the anti-icing module for each heater power respectively by setting the LWC to 0 g/m^3.

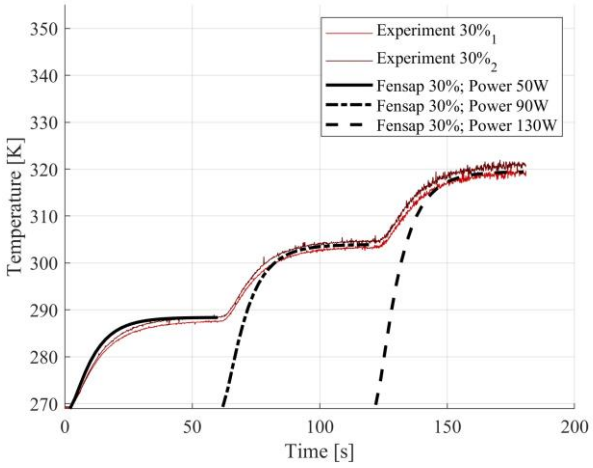

Fig. 12 Comparison of internal temperature to experimental test case #2 (-5°C) for 30% section.

The additional time required for the 90 W and 130 W cases compared to the experiments is clearly visible. Nevertheless, similarly to the wet test cases, the biggest deviations occur during the temperature rise in the material. Good agreement between the results is observable when steady-state temperatures are reached. Furthermore, an interesting difference emerges when comparing the data of test case #1 with that of test case #2, both at a temperature of −5 °C but with different LWC. The first 60 s of test case #2 the heater is powered with 50 W, whereas in test case #1 the heater is powered with 70 W. When comparing an investigated propeller section, the reached internal temperature in test case #2 is always higher than for test case #1. This might be a first indicator of differences between cases where only convection occurs (case #2), and cases where convection and evaporation occurs (case #1), when more heat is dissipated at the surface of the propeller in the area of the ETIPS. Further analysis of that can be found in the following.

C. The effects of flow and icing conditions

To understand the occurring aerodynamic and thermodynamic phenomena, properties like the HTC and heat fluxes (HF) are analyzed. The difference in total temperatures achieved between the three propeller sections can be observed by the comparison of the three HTCs as shown in Fig. 13.

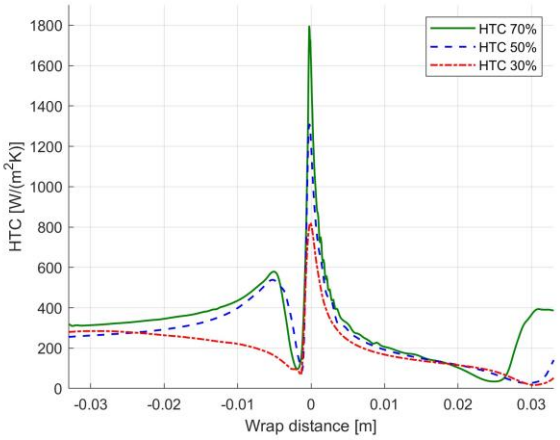

Fig. 13 Comparison of HTC between propeller sections using FENSAP-ICE results.

The 70% section has the biggest radial distance from the propeller hub and therefore the biggest relative speed, followed by the 50% and 30% sections. This results in the highest inflow velocity at the leading edge for the 70% section and therefore highest convection cooling at that point, which leads to the highest peak value of the HTC.

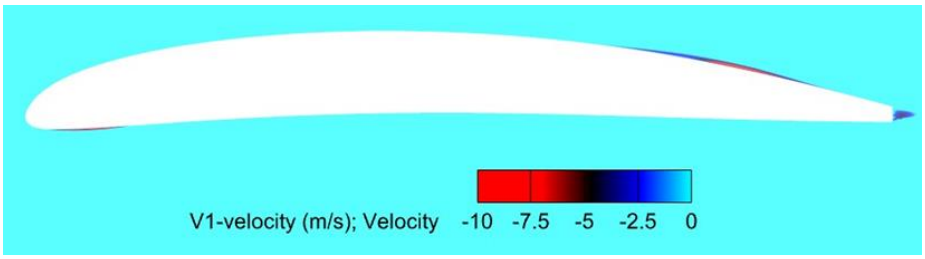

Fig. 14 Visualization of separation bubbles at the 70% propeller section on the suction side.

The drops of the HTC at around −0.002 m and 0.025 m are in accordance to flow separations and detachment areas, visible in Fig. 14 In general, each of the three propeller sections shows individual flow characteristics due to the difference in AOA and rotation rate. The most pronounced effects are observable at the 70% section because of the highest inflow speed and therefore in the following, some results are discussed at the 70% section only.

Regarding the heat fluxes of test cases #1, the separation between convection and evaporation is clearly visible. Evaporation and convection are the two most influencing heat fluxes on the propeller surface. Fig. 15 shows the convective, evaporative and the sum of both over the propeller surface. Additionally, the caught water is shown on the right y-axis as well.

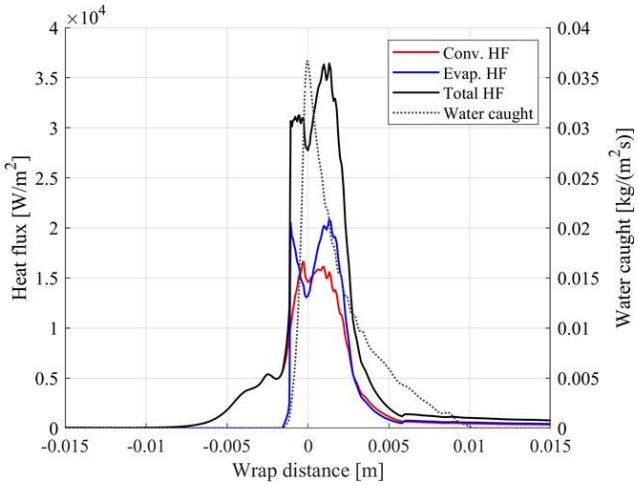

Fig. 15 Heat fluxes of test case #1 at the 70% section.

At locations without a water film or impinging water droplets, no evaporation can be found and only convection occurs. Furthermore, the evaporative heat flux at the impinging zone reaches higher values than the convective one but drops further than the convective one at the location where most water impinges. The convective heat flux on the other hand stays constant or even experiences a slight rise at the leading edge. In addition, the total heat flux becomes almost zero at the surface locations where the heat generated from inside is insufficient and the surface temperature drops to almost 0 °C. By quantifying the evaporative and convective heat flux above the whole propeller surface it was found that for test case #1 the convective heat flux reaches 88.35 W/m and the evaporative one 75.67 W/m, which corresponds to 53.87% and 46.13%.

For a deeper understanding of the differences between the convective and evaporative heat fluxes, comparisons between the wet test case #1 and dry test case #2 are necessary, also taking into account the surface temperatures, as shown in Fig. 16. Presented are the test cases at −5 °C and the first 60 s of the dry test case #2. Additionally, a further simulation is shown under dry conditions with a heater power of 70 W as in the test case #1. The smallest values in the droplet-impinging zone are found for the wet test case when evaporation is present as well. Increased for the dry cases according to the heater power. Considering the wet case and dry case powered with 70 W, the dry case reaches much higher values right at the stagnation point and the heat flux is sharpened. The total HF of the wet case does not reach such high values but covers a larger area (−0.0020 m - 0.0025 m) than the dry HF due to the water movement and the heat conduction in the water along the surface, which transfers the heat away from the stagnation point.

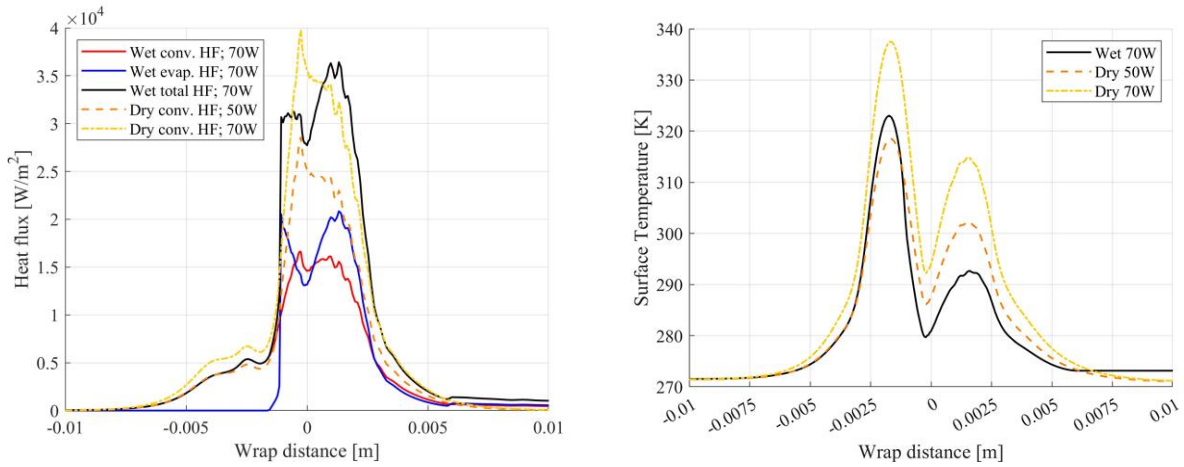

a) **b)**

Fig. 16 Comparison of heat fluxes a) and surface temperatures b) between wet and dry test cases at the 70% section.

Furthermore, the surface temperature in the impinging zone of test case #1 is lower compared to test case #2, despite the higher power of the wet test case #1. This also applies to cases where wet and dry conditions are each operated with 70 W. The temperature peak on the upper leading edge is at the location where for the wet test case a water film is present at the surface. The peak on the lower side aligns with the location where the separation bubble was observed, leading to a decrease in HTC and preventing the water film from entering this area. Only convection is present for all test cases.

Finally, a different surface temperature behavior can be seen on the upper surface behind the heated area when surface temperatures of around 0 °C occur. For the dry cases, the temperature drops below the freezing point immediately, whereas for the wet case a constant surface temperature can be seen at around the freezing point. This agrees with the location of runback ice accretion. Hence, latent heat keeps the surface at around the freezing point for the wet case. Nevertheless, the comparison of the maximal internal temperatures shows that the highest temperature of 68.65 °C is reached for the dry case with 70 W followed with 52.86 °C for the wet test case #1 and 48.40 °C for the dry test case #2 at 50 W heater power.

D. IPS optimization

After validating the numerical simulations by experimental tests, the results are used to optimize the IPS design with regard to efficiency. The new designs are numerically tested in accordance with the experimental conditions of test cases #1 and #3. The previous results with the original ETIPS design of one heating pad in the leading edge revealed some weaknesses. Even with maximum power of the ETIPS and overshooting the internal temperature limit, the heat conductivity to the back of the propeller along the surface was insufficient and runback ice always accumulated.

Regarding the aspect of runback ice on the upper surface of the propeller, the first improving concept is to implement more ETIPS modules along the surface of the propeller as shown in Fig. 17. The idea is to keep more of the upper surface above the freezing temperature of 0 °C. Five additional modules, each the length of 5.730 mm and the height of 0.215 mm are integrated between the glass fiber layers just like the original ETIPS module in the leading edge. The unidirectional carbon is not twisted in the additional integrated heaters as it is for the single leading edge heater. Hence, these heater elements have anisotropic properties and an equivalent height of 0.200 mm with an equivalent conductivity of 0.693 W/(mK) was calculated.

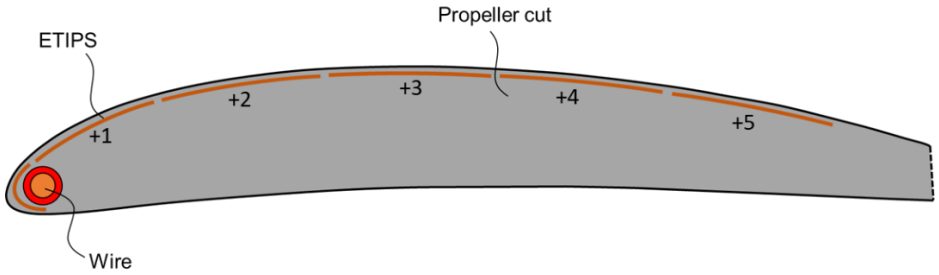

Fig. 17 Schematic sketch of additional heater pads along the surface.

Numerical tests on the 70% and 30% sections showed that four additional heaters are necessary to avoid any accretion of runback ice. This can be seen in Fig. 18 that the surface temperature does not build a plateau anymore. For further analysis, the four additional heater pads were powered equally as one big heat pad to keep the design and functionality as simple as possible in a manufacturing aspect.

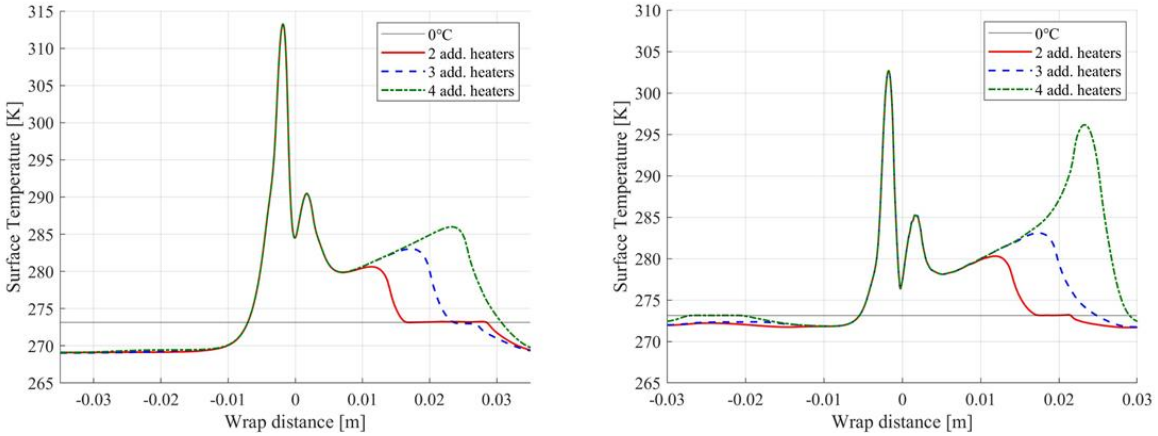

Fig. 18 Surface temperature at 30% section a) and 70% section b) for test case #1 with different amount of additional heaters.

Regarding the area of the leading edge, the 30% section reaches the highest temperatures as already previously discovered due to the rather steep inflow and slowest relative speed. The temperature along the upper surface due to the additional heaters increases with a constant gradient. This is not the case for the 70% section and four heaters. An extreme peak of the surface temperature at the fourth heater position develops. This is due to the flow detachment in this area where even backflow appears, which is in good agreement with the HTC as can be seen in Fig. 13. Heat extraction is damped and the temperature increases unproportioned since neither evaporation nor convection can extract heat in this case.

Considering the cases when only two heaters are powered, the surface temperature does not immediately drop below zero degrees behind the second heater. It remains a few millimeters around the freezing point. This is due to the latent heat that is released and heats the surface when water changes its phase from liquid to solid.

One outcome of the analyzed results is that the most critical spot with the highest temperature development is still in the leading edge where the highest power is necessary due to the impinging droplets. The rather high thermal resistive layers around the leading edge heaters are also not beneficial. A rather abstract consideration is done by applying a copper layer in the propeller structure to show the influence of a reduced heat resistance layer. Therefore, the original propeller setup with just one heater pad in the leading edge was taken. In the numerical setup, the outer glass fiber layer is then applied with the material values of copper according to Table 4.

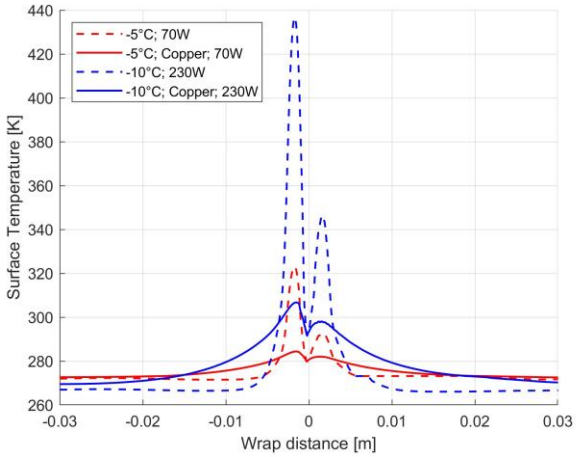

Fig. 19 Surface temperatures of test cases #1 and #3 with and without copper layer.

Compared to glass fiber, copper has a much higher heat conductivity, higher density and a smaller value of the specific heat. The results in Fig. 19 show an improved temperature distribution due to the higher heat conductivity and less heat resistivity. Thus, a reduced maximal internal and surface temperature occurs. Due to the improved heat transfer in the copper layer along the surface, the flattening of the temperature along the surface is longer and the surface is kept above the freezing point in a larger area. In general, the maximal internal temperature could be reduced for test case #1 from 52.86 °C to 28.1 °C and for test case #3 from 173.14 °C to 88.75 °C. Even that thin copper layer of just 0.06 mm not only improves the prevention of ice accretion, but also reduces the heat impact on the internal structure by distributing the heat internally much faster and more efficiently.

V. Discussion

A. Validation of 2D CHT-propeller simulations with experiments

Overall, the numerical results agree well with the experimental data, especially when steady-state is reached, as can be seen in Fig. 10. First, considering only the experimental data. The differences in blades for the 30% section might be caused by uneven appearance of runback ice behind the heated zone of the two blades, which was observed during the experiments. This is most likely caused by small surface impurities or flow field variations. For the 50% section in both cases, a similar gap occurs between the blades. This might rather indicate manufacturing inaccuracies when the thermistors are not placed in the exact same positions. A further cause could be an imbalance between the heating elements of the IPS causing different power outputs in each blades.

Comparing the numerical simulations with the experimental data, the biggest observable difference between the numerical and experimental results can be seen in the temperature gradient within the first 15 s - 20 s of the tests. This applies to all cases. The steady temperature is reached in the numerical results faster than in the experiments. Material properties such as density, specific heat and thermal conductivity have the greatest influence on how fast heat is transferred through a solid. The heater power and with it the temperature difference that forces heat conduction has an influence as well. The power is known from the test execution, so the uncertainty of the material values is more likely. Nevertheless, when steady-state of the temperatures are reached all numerical simulations are in very good agreement with the experimental data.

B. The effects of flow and icing conditions

The comparison of the HTC for the three sections shows the differences in the relative speeds of the sections. Beginning from the tip of the leading edge, for all three cases, the flow has a laminar structure and starts to build up a boundary layer. Along the upper surface, the HTC decreases similarly in all cases as typical for laminar boundary layers. The boundary layer heats up with the distance and the temperature difference between liquid and surface decreases. The heat transfer is dependent on the temperature difference and is therefore lower over the distance. Locations where the HTC drops to almost zero with a followed rise are visible for example at the lower leading edge and at the upper rear part. The drops indicate positions where the flow starts to detach due to the curvature of the propeller surface as shown in Fig. 14. In the detachment area, backflow occurs and the flow transits from a laminar to a turbulent characteristic. The rise in the HTC afterwards shows the region where the turbulent flow reattaches and

heat is transferred more efficiently again. Due to the rather steep negative AOA for the 30% section, the separation bubble is along the complete lower surface of the propeller and the flow does not re-attach but rather forces backflow. For the 50% and 70% sections, the flow re-attaches almost immediately with a turbulent characteristic. This causes the rise in HTC at that position and is followed again by a slight reduction along the surface due to the development of a boundary layer.

Several effects and thermodynamic aspects can be discussed by analyzing the heat fluxes of convection and evaporation. Since evaporation requires a liquid, it only occurs at locations where a water film is present. Evaporation depends mainly on temperature. Heat is the required energy for the phase change from liquid to gas. Furthermore, the evaporative heat flux at the impinging zone reaches higher values than the convective one. This might be due to the better heat exchange between water and solid than air and solid, which causes a more efficient heating of the water film. In these cases, more energy goes into latent heat. Indications for that are due to general lower values of the convective heat flux in areas where water occurs, visible in Fig. 15 and Fig. 16. Interesting is the drop of the evaporative heat flux at the stagnation point at the leading edge. At this point the highest amount of water impingement on the surface is reached. At the stagnation point, effects such as impingement cooling and forced convection must be taken into account. As cold water droplets come into contact with the heated surface, heat is transferred into the water due to the temperature difference between the surface and the cold water. However, despite this heat transfer, the energy extracted at the leading edge is not sufficient to instantly evaporate the continuous stream of droplets and a water film occurs. Due to the shear stress, the airflow along the surface initiates the movement of the water film and leads to the smallest thickness at the leading edge. The ongoing stream of cold water droplets on the leading edge constantly extracts heat. The heat flux increases again downstream when the extracted heat is sufficient to cause evaporation.

Convection on the other hand is treated by temperature difference between surface and air or a high HTC. While the surface temperature reaches a minimum at the leading edge due to the impinging droplets, the HTC reaches its maximal values, comparing Fig. 13 and Fig. 16. This peak value is due to the flow at the stagnation point when convection is forced the most. The particles extract heat and increase the internal energy. Due to the high speed of the air flow, these particles are moved away from the surface much faster and space is created for new particles, which can extract more heat. Along the upper surface, the surface temperature reaches a local maximum, which prevents the heat flux from dropping even though the HTC decreases. The second surface temperature peak at the lower leading edge is caused by a separation bubble area. The heat transfer away from the surface is damped. In this area, no water impinges and only convection occurs for all test cases. On the one hand, this shows that with higher heater power the surface is heated even more. On the other hand, in the two cases with 70 W (Fig. 16), the influence of water and evaporation is also visible at the surface spots where no water is present. At the upper leading edge, the heat transfer is increased for the wet case, resulting in a lower surface temperature. The result is a greater temperature difference between these surface points and the IPS heater. This leads to a greater heat conduction and heat flux that is mainly forced by the temperature difference. Consequently, less heat is internally transferred to the lower surface despite the same heating power, resulting also in different surface temperatures.

C. Optimization

Both concepts show numerically interesting results in achieving lower temperature peaks and bigger areas that are free of ice. These tests again neglect the effects on the strength and stability properties of the propeller or the manufacturing possibilities. The biggest problem occurs due to the electrical conductivity of copper that is directly in contact with the powered heater pad. In addition, copper has a higher density than composite materials and therefore has a greater impact on the propeller weight. Further studies are required for the practical possibilities and applications, but the results obtained show that it might be worthwhile to pursue these ideas further.

D. Uncertainties

In this work, experimental and numerical uncertainties need to be taken into account for the analysis of the results. In manufacturing, minor variations in material, sensor positions, and ambient conditions lead to discrepancies. Even identical propellers differ. Experimental tests in an icing wind tunnel face changing flow, icing conditions, and humidity, affected by small amounts of ice accretion on the nozzles or walls. Instruments have limited accuracy due to calibration and sensor issues. Steps taken for highly reliable results include monitoring nozzle flow, pre-run calibrations, post-ice cleaning, and repetitions to minimize uncertainties. Previous destructive tests ensure acceptable propeller variations.

Considering numerical aspects, uncertainties arise from user-defined start conditions and numerical parameters. Turbulent model choice, especially the k-ω SST model, and HTC calculation using the EID model introduce uncertainties due to lack of experimental verification. Inconsistent droplet distribution during icing experiments may

lead to discrepancies with simulations using average LWC. Material property uncertainties in composite propeller layup affect temperature gradients and necessitate a detailed study for accurate assessment. Grid generation, like wire position, poses uncertainties, potentially influencing internal temperature distribution. To mention is also the simplification introduced by looking at 2D sections instead of 3D models, neglecting 3D effects. Despite these challenges, numerical results surprisingly align well with experimental data, suggesting that uncertainties might be less impactful due to careful analysis and accurate assumptions aligned with real experimental conditions.

VI. Conclusion

This study investigated the anti-icing capabilities of a fixed-wing UAV propeller ice protection system. The small-medium sized UAV considered has a maximum take-off weight of about 25 kg. The system utilizes resistive heating, belonging to the category of electro-thermal ice protection systems. The IPS design was examined through experimental validation and numerical simulations to evaluate its efficiency in preventing ice accretion while considering its impact on aerodynamic and thermodynamic factors. The goal was to optimize the system without exceeding the critical glass transition temperature of 60 °C of the resin in the composite propeller.

Experimental tests conducted in an icing wind tunnel simulated various flight conditions. Internal temperature measurements along the propeller radius revealed insights into thermal behaviour, radial distance influence, and runback ice issues. The results indicated high efficiency at the leading edge but weaknesses along the upper surface, leading to runback ice.

Numerical simulations using computational fluid dynamics and conjugate heat transfer methods validated by experimental results and literature data provided a detailed analysis of flow phenomena, temperature distributions, and heat transfer mechanisms. Factors such as detachments and laminar-turbulent transitions were considered, deepening the understanding of thermal distribution patterns. Optimization efforts, including additional heaters along the upper surface and integrating a copper layer for enhanced heat conductivity, yielded promising results in preventing runback ice and expanding operational parameters.

In conclusion, this study presents a comprehensive analysis of an electro-thermal ice protection system for UAV propellers based on experimental and numerical investigations. The simulations with ANSYS FENSAP-ICE have been validated to ensure reliable predictions of the internal temperatures of an ETIPS. The findings offer valuable insights into thermal effects on composite structures during in-flight anti-icing. By addressing thermodynamic and aerodynamic aspects, optimization strategies were identified, ensuring both external anti-icing requirements and internal temperature limits were met. These results provide a robust and reliable solution for UAV propeller anti-icing, enabling safe operations in challenging weather conditions, particularly in remote areas where UAVs play a vital role in providing medical and emergency care.

Acknowledgments

The numerical simulations were performed on resources provided by the National Infrastructure for High Performance Computing and Data Storage in Norway (UNINETT Sigma2) on the Fram supercomputer, under project code NN9613K Notur/NorStore. The work is sponsored by the Research Council of Norway through an Industrial PhD with project number 321667 and project IKTPLUSS with project number 316425.

References

[1] N. C. Müller and R. Hann, UAV Icing: 3D Simulations of Propeller Icing Effects and Anti-Icing Heat Loads, SAE Technical Paper 2023-01-1383, 2023. DOI: 10.4271/2023-01-1383.

[2] R. Hann and T. A. Johansen, Unsettled Topics in Unmanned Aerial Vehicle Icing, SAE EDGE Research, 2020. DOI: 10.4271/EPR2020008.

[3] P. Mátyás and N. Máté, Brief history of UAV development, Repüléstudományi Közlemények, vol. 31, no. 1, pp. 155-166, 2019. DOI: 10.32560/rk.2019.

[4] H. Shakhatreh, A. H. Sawalmeh, A. Al-Fuqaha, Z. Dou, E. Almaita, I. Khalil, N. S. Othman, A. Khreishah and M. Guizani, Unmanned Aerial Vehicles (UAVs): A Survey on Civil Applications and Key Research Challenges, IEEE Access, vol. 7, pp. 48572-48634, 2019. DOI: 1109/ACCESS.2019.2909530.

[5] O. Bünte, MIT-Drohnenunternehmen Aviant startet Lieferservice Kyte in Norwegen, heise online, https://www.heise.de/news/MIT-Drohnenunternehmen-Aviant-startet-Lieferservice-Kyte-in-Norwegen-9179776.html, 2023.

[6] M. J. van Veelen, G. Roveri, A. Voegele, T. D. Cappello, M. Masè, M. Falla, I. B. Regli, A. Mejia-Aguilar, S. Mayrgündter and G. Strapazzon, Drones reduce the treatment-free interval in search and rescue operations

with telemedical support - A randomized controlled trial, The American Journal of Emergency Medicine, vol. 66, pp. 40-44, 2023. DOI: 1016/j.ajem.2023.01.020.
[7] B. C. Bernstein and C. Le Bot, An Inferred Climatology of Icing Conditions Aloft, Including Supercooled Large Drops. Part II: Europe, Asia, and the Globe, Journal of Applied Meteorology and Climatology, vol. 48, no. 8, pp. 1503-1526, 2009. DOI: 1175/2009JAMC2073.1.
[8] R. Hann, Atmospheric Ice Accretions, Aerodynamic Icing Penalties, and Ice Protection Systems on Unmanned Aerial Vehicles, PhD Thesis NTNU2020:200, Norwegian University of Science and Technology, 2020.
[9] M. Lindner, J. Wallisch and R. Hann, UAV Icing: Numerical Simulation of Icing Effects on Wing and Empennage, SAE Technical Paper 2023-01-1384, 2023. DOI: 10.4271/2023-01-1384, 2023.
[10] R. W. Gent, N. P. Dart and J. T. Cansdale, Aircraft icing, Philosophical Transactions of the Royal Society of London. Series A: Mathematical, Physical and Engineering Sciences, no. 358, pp. 2873-2911, 2000. DOI: 1098/rsta.2000.0689.
[11] E.W. Brouwers, J.L. Palacios, E.C. Smith and A.A. Peterson, The experimental investigation of a rotor hover icing model with shedding, 1st ed.Phoenix, AZ: American Helicopter Society 66th Annual Forum, 2010.
[12] R. Hann and T. A. Johansen, UAV icing: the influence of airspeed and chord length on performance degradation, Aircraft Engineering and Aerospace Technology, vol. 93, no. 5, pp. 832-841, 2021. DOI: 10.1108/AEAT-06-2020-0127.
[13] R. J. Flemming, A History of Ice Protection System Development at Sikorsky Aircraft, SAE Technical Paper Series, 2003. DOI: 10.4271/2003-01-2092.
[14] R. Hann, N. Müller, M. Lindner and J. Wallisch, UAV Icing: Experimental Validation Data for Predicting ice Shapes at Low Reynolds Numbers, SAE Technical Paper 2023-01-1372, 2023. DOI: 10.4271/2023-01-1372.
[15] H. Heramarwan, N. Müller, R. Hann and T. Lutz, UAM Icing: Ice Accretion Experiments and CFD Icing Simulations on Rotors for eVTOL Unmanned Aircraft, SAE Technical Paper 2023-01-1391, 2023. DOI: 10.4271/2023-01-1391.
[16] B. Løw-Hansen, N. C. Müller, E. M. Coates, T. A. Johansen and R. Hann, Identification of an Electric UAV Propulsion System in Icing Conditions, SAE Technical Paper 2023-01-1378, 2023. DOI: 10.4271/2023-01-1378.
[17] N. C. Müller, B. Løw-Hansen, K. T. Borup and R. Hann, UAV icing: Development of an ice protection system for the propeller of a small UAV, Cold Regions Science and Technology, 2023. DOI: 1016/j.coldregions.2023.103938.
[18] N. C. Müller and R. Hann, UAV Icing: A Performance Model for UAV Propeller in Icing Conditions, AIAA AVIATION 2022 Forum, pp. 1-17, 2022. DOI: 2514/2022-3903.
[19] O. Fakorede, Z. Feger, H. Ibrahim, A. Ilinca, J. Perron and C. Masson, Ice protection systems for wind turbines in cold climate: characteristics, comparisons and analysis, Renewable and Sustainable Energy Reviews, vol. 65, pp. 662-675, 2016. DOI: 1016/j.rser.2016.06.080.
[20] É. Villeneuve, A. Samad, C. Volat, M. Béland and M. Lapalme, Experimental assessment of the ice protection effectiveness of icephobic coatings for a hovering drone rotor, Cold Regions Science and Technology, vol. 210, pp. 103-858, 2023. DOI: 1016/j.coldregions.2023.103858.
[21] R. Hann, A. Enache, M. C. Nielsen, B. N. Stovner, J. van Beeck, T. A. Johansen and K. T. Borup, Experimental Heat Loads for Electrothermal Anti-Icing and De-Icing on UAVs, Aerospace, vol. 8, no. 83, pp. 1-15, 2021. DOI: 10.3390/aerospace8030083.
[22] K. K. Chawla, Composite materials. Science and engineering, 3. ed.New York, Heidelberg: Springer, 2012. DOI: 1007/978-0-387-74365-3.
[23] N. A. Grunina, T. V. Belopolskaya and G. I. Tsereteli, The glass transition process in humid biopolymers. DSC study, Journal of Physics: Conference Series, vol. 40, pp. 105-110, 2006. DOI: 1088/1742-6596/40/1/013.
[24] Q. Xue, C. Lv, M. Shan, H. Zhang, C. Ling, X. Zhou and Z. Jiao, Glass transition temperature of functionalized graphene–polymer composites, Computational Materials Science, vol. 71, pp. 66-71, 2013. DOI: 1016/j.commatsci.2013.01.009.
[25] R. Hann, (2023). Numerical Simulation of In-Flight Icing of Unmanned Aerial Vehicles. In: Habashi, W.G. (eds) Handbook of Numerical Simulation of In-Flight Icing. Springer, Cham. DOI: 10.1007/978-3-030-64725-4_12-1 .
[26] ANSYS, Inc., Ansys FENSAP-ICE User Manual, no. 22.2, 2022.
[27] H. Beaugendre, F. Morency and W. G. Habashi, Development of a Second Generation In-Flight Icing Simulation Code, Journal of Fluids Engineering, vol. 128, no. 2, pp. 378-387, 2006. DOI: 1115/1.2169807.

[28] Y. Bourgault, W. G. Habashi, J. Dompierre and G. S. Baruzzi, A finite element method study of Eulerian droplets impingement models, International Journal for Numerical Methods in Fluids, vol. 29, no. 4, pp. 429-449, 1999. DOI: 1002/(SICI)1097-0363(19990228)29:4<429:AID-FLD795>3.0.CO;2-F.
[29] H. Beaugendre, F. Morency and W. G. Habashi, FENSAP-ICE's Three-Dimensional In-Flight Ice Accretion Module: ICE3D, Journal of Aircraft, vol. 40, no. 2, pp. 239-247, 2003. DOI: 2514/2.3113.
[30] G. Croce, H. Beaugendre and W. Habashi, CHT3D - FENSAP-ICE conjugate heat transfer computations with droplet impingement and runback effects, 40th AIAA Aerospace Sciences Meeting, 2002. DOI: 10.2514/6.2002-386.
[31] "Airfoil Tools," [Online]. Available: http://airfoiltools.com/index. [Accessed 11 July 2023].
[32] "Mejzlik.eu - Design and manufacturing top-quality propellers," [Online]. Available: https://www.mejzlik.eu/. [Accessed 11 July 2023].
[33] "NX software | Siemens Software," Siemens Digital Industries Software, [Online]. Available: https://plm.sw.siemens.com/de-DE/nx/. [Accessed 11 July 2023].
[34] "Pointwise for Computational Fluid Dynamics Meshing," [Online]. Available: https://www.cadence.com/en_US/home/tools/system-analysis/computational-fluid-dynamics/pointwise.html. [Accessed 2 October 2023].
[35] P. J. Roache and P. M. Knupp, Completed Richardson extrapolation, Communications in Numerical Methods in Engineering, vol. 9, no. 5, pp. 365-374, 1993. DOI: 1002/cnm.1640090502.
[36] T. O. Hodson, Root-mean-square error (RMSE) or mean absolute error (MAE): when to use them or not, Geoscientific Model Development, vol. 15, no. 14, pp. 5481-5487, 2022. DOI: 10.5194/gmd-15-5481-2022.
[37] T. Ohmura, M. Tsuboi and T. Tomimura, Estimation of the Mean Thermal Conductivity of Anisotropic Materials, International Journal of Thermophysics, vol. 23, no. 3, pp. 843-853, 2002. DOI: 1023/A:1015423708823.
[38] K. Dong, B. Gu and B. Sun, Comparisons of thermal conductive behaviors of epoxy resin in unidirectional composite materials, Journal of Thermal Analysis and Calorimetry, vol. 124, no. 2, pp. 775-789, 2016. DOI: 1007/s10973-015-5197-5.
[39] H. Zhang, W.-Z. Fang, Y.-M. Li and W.-Q. Tao, Experimental study of the thermal conductivity of polyurethane foams, Applied Thermal Engineering, vol. 115, pp. 528-538, 2017. DOI: 1016/j.applthermaleng.2016.12.057.
[40] H. Zhang, K. Wu, G. Xiao, Y. Du and G. Tang, Experimental study of the anisotropic thermal conductivity of 2D carbon-fiber/epoxy woven composites, Composite Structures, vol. 267, p. 113870, 2021. DOI: 1016/j.compstruct.2021.113870.
[41] "Laminate Calculator - R&G Faserverbundwerkstoffe GmbH," [Online]. Available: https://www.r-g.de/en/laminatecalculator.html. [Accessed 24 July 2023].
[42] W. Johnson, Helicopter Theory, Dover Publications, 2012.
[43] T. Mikko, J. Tuomas, M. Lasse and B. Geert-Jan, VTT Icing wind tunnel 2.0, Winterwind Presentations 2016, 2016.
[44] "Series 1780: Drone Thrust Stand," T. Robotics, [Online]. Available: https://www.tytorobotics.com/pages/series-1780. [Accessed 31 July 2023].
[45] KONTRONIK - Hochleistungsantriebe im RC-Modellbau.
[46] "Q80-9M V2 kv160 | Hacker Q80 | Hacker Außenläufer | Elektromotoren," [Online]. Available: https://www.hacker-motor-shop.com/Elektromotoren/Hacker-Aussenlaeufer/Hacker-Q80/Q80-9M-V2-kv160.htm?SessionId=&a=article&ProdNr=37418022&p=2986. [Accessed 31 July 2023].
[47] "GHS38109 series High Speed Slip Ring(+Electric Slip Rings) - MOFLON," [Online]. Available: https://www.moflon.com/ghs38109.html. [Accessed 31 July 2023].
[48] D. Miller, T. Bond, D. Sheldon, W. Wright, T. Langhals, K. Al-Khalil and H. Broughton, Validation of NASA thermal ice protection computer codes. I - Program overview, 35th Aerospace Sciences Meeting and Exhibit, 1997. DOI: 10.2514/6.1997-49.
[49] W. Wright, K. Al-Khalil and D. Miller, Validation of NASA thermal ice protection computer codes. II - LEWICE/Thermal, 35th Aerospace Sciences Meeting and Exhibit, 1997. DOI: 10.2514/6.1997-50.
[50] K. Al-Khalil, C. Horvath, D. Miller and W. Wright, Validation of Thermal Ice Protection Computer Codes: Part 3- The Validation of ANTICE, 35th Aerospace Sciences Meeting and Exhibit, 1997. DOI: 10.2514/6.1997-51.
[51] A. Carozza, F. Petrosino and G. Mingione, Numerical procedure for the simulation of an electro-thermal anti-icing system, Aircraft Engineering and Aerospace Technology, vol. 94, no. 8, pp. 1433-1448, 2022, DOI: 10.1108/AEAT-07-2021-0222.